instruments

MDPI

Article

Impact of Superconductors' Properties on the Measurement Sensitivity of Resonant-Based Axion Detectors

Andrea Alimenti [1,*], Kostiantyn Torokhtii [1], Daniele Di Gioacchino [2], Claudio Gatti [2], Enrico Silva [1,3] and Nicola Pompeo [1,3]

[1] Dipartimento di Ingegneria Industriale, Elettronica e Meccanica, Università degli Studi Roma Tre, Via Vito Volterra 62, 00146 Roma, Italy; kostiantyn.torokhtii@uniroma3.it (K.T.); enrico.silva@uniroma3.it (E.S.); nicola.pompeo@uniroma3.it (N.P.)

[2] INFN, Laboratori Nazionali di Frascati, 00044 Frascati, Italy; daniele.digioacchino@lnf.infn.it (D.D.G.); claudio.gatti@lnf.infn.it (C.G.)

[3] INFN, Sezione Roma Tre, 00146 Roma, Italy

* Correspondence: andrea.alimenti@uniroma3.it

Abstract: Axions, hypothetical particles theorised to solve the strong CP problem, are presently being considered as strong candidates for cold dark matter constituents. The signal power of resonant-based axion detectors, known as haloscopes, is directly proportional to their quality factor Q. In this paper, the impact of the use of superconductors on the performances of haloscopes is studied by evaluating the obtainable Q. In particular, the surface resistance R_s of NbTi, Nb_3Sn, $YBa_2Cu_3O_{7-\delta}$, and $FeSe_{0.5}Te_{0.5}$ is computed in the frequency, magnetic field, and temperature ranges of interest, starting from the measured vortex motion complex resistivity and the screening lengths of these materials. From R_s, the quality factor Q of a cylindrical haloscope with copper conical bases and a superconductive lateral wall, operating with the TM_{010} mode, is evaluated and used to perform a comparison of the performances of the different materials. Both $YBa_2Cu_3O_{7-\delta}$ and $FeSe_{0.5}Te_{0.5}$ are shown to improve the measurement sensitivity by almost an order of magnitude, with respect to a whole Cu cavity, while NbTi is shown to be suitable only at lower frequencies (<10 GHz). Nb_3Sn can provide an intermediate improvement of the whole spectrum of interest.

Keywords: axion detector; haloscope; microwaves; superconductors; surface impedance; vortex motion; anisotropy; pinning

Citation: Alimenti, A.; Torokhtii, K; Di Gioacchino, D.; Gatti, C.; Silva, E.; Pompeo, N. Impact of Superconductors' Properties on the Measurement Sensitivity of Resonant-Based Axion Detectors. *Instruments* **2022**, *6*, 1. https://doi.org/10.3390/instruments6010001

Academic Editors: Andrea Messina and Gianluca Lamanna

Received: 30 November 2021
Accepted: 27 December 2021
Published: 30 December 2021

1. Introduction

The axion is a particle associated with the dynamic field introduced by Peccei–Quinn in 1977 [1–3] to solve the 'strong CP problem', i.e., the missing experimental observation of the CP symmetry violation foreseen by the quantum chromodynamics theory. The characteristics of this particle also make it particularly appealing for the resolution of another unsolved physical problem: the nature and existence of dark matter. Thus, in the last years, a strong interest emerged in the experimental detection of axions.

Due to the small cross section of axions with the ordinary baryonic matter and with photons, the different detection approaches exploit the Primakoff effect [4]—that is, the conversion of axions into photons in the presence of high magnetic fields B. The frequency of the produced photons γ_{ph} is $\nu = E_{ph}/h$, with E_{ph} being the total energy of the particle (including the rest mass energy and the kinetic contribution) and h being the Planck constant. Thus, $E_{ph} = m_a c^2 + \frac{1}{2} m_a v^2$, where m_a is the mass of the axions, c is the speed of light in vacuum, and v is the particle speed, which, for axions compatible with the cold dark matter properties, is $<10^{-3}c$ [5]. Hence, in practice, $E_{ph} \approx m_a c^2$. m_a is constrained by astronomical and cosmological considerations in the interval $1 < m_a/(\mu\text{eV}) < 10^3$ [5–8]. Hence, $2 \times 10^8 \leq \nu/(\text{Hz}) \leq 2 \times 10^{11}$.

In 1983, P. Sikivie [9] proposed an experimental test for the existence of axions based on the use of resonant microwave cavities, known as haloscopes. When the axions enter

the cavity, they can be converted into microwave photons by externally generated B fields, and in this way, they can be detected using very low-noise electronics [10]. The signal power $P_{a\to\gamma_{ph}}$ to be detected is shown to be [9,10]:

$$P_{a\to\gamma_{ph}} \propto \left(B^2VQ\right)\left(g^2_{a\gamma_{ph}}\rho_a\nu\right), \quad (1)$$

where V is the volume of the cavity, Q is the quality factor, $g_{a\gamma}$ is the axion–photon coupling, and ρ_a is the local density of axions. On the basis of existing experiments, one finds $10^{-23} < P_{a\to\gamma_{ph}}/(\mathrm{W}) < 10^{-22}$. In the proportionality statement (1), the terms in the right brackets do not depend on human will. Thus, the only change to improve the signal power, in order to reduce the integration time, consists in the optimisation of the parameters in the left set of brackets in (1).

The high Q needed to increase $P_{a\to\gamma_{ph}}$ pushes toward the study of new methods to reduce the cavity losses. The best results are obtained with either superconductive [11–13] or dielectric resonant cavities [14,15]. Since, in metallic cavities, $Q \propto R_s^{-1}$, R_s being the surface resistance of the conductive walls of the cavity, materials with low R_s must be employed. Beyond copper, only superconductive materials can be explored. However, the choice is not obvious, since when superconductors (SC) are used at high frequencies and in high magnetic fields, they are driven in the mixed state so that large losses emerge due to the dissipative motion of fluxons. Fluxons are quanta of magnetic flux, of amplitude $\Phi_0 = h/(2e) \approx 2.068 \times 10^{-15}$ Wb, that penetrate type-II superconductors in the presence of the high magnetic field levels needed for the haloscopes (i.e., of the order of some tesla). In these conditions, the R_s of technological superconductors is dominated by the electrodynamics of fluxons. The latter must then be accurately characterised in order to assess the suitability of these materials for the realisation of highly sensitive haloscopes.

Different superconductive haloscopes have been recently developed and tested. In [11], the Q-factor of copper and NbTi haloscopes (tuned at ∼9.08 GHz) have been measured, showing that, with a NbTi cavity, the figure of merit B^2Q at ∼6 T is five-times larger than what is reached with a Cu cavity. The first RE-$Ba_2Cu_3O_{7-\delta}$ (RE-BCO) cavity, with RE being a rare earth element such as Y, was shown in [12] to exhibit $Q \approx 3.25 \times 10^5$ at 6.93 GHz and up to 8 T, which is more than six-times larger than that obtained with a Cu cavity. Recently, in [13], a different configuration for a RE-BCO cavity was presented, and its performances compared with one coated with Nb_3Sn, both working at ∼9 GHz: the RE-BCO haloscope reached $Q \sim 7 \times 10^4$ at ∼12 T, which was shown to be only 1.75-times larger than that obtained with the equivalent Cu cavity. Moreover, the Q-factor of the Nb_3Sn cavity showed a strong field dependence that apparently prevents the use of this material for these kinds of applications.

In this paper, the most promising superconductors for resonant axion detectors, i.e., Nb_3Sn, NbTi, $YBa_2Cu_3O_{7-\delta}$ (YBCO), and, as a perspective, $FeSe_{0.5}Te_{0.5}$ (FeSeTe), are considered. Their R_s is evaluated in the expected operative conditions of haloscopes, starting from the studies of the vortex motion properties performed on these materials. In particular, the data used to perform the analysis on Nb_3Sn and NbTi are taken, respectively, from [16,17], whereas those used to analyse the performances of YBCO and FeSeTe were measured specifically for this study. From R_s, the figures of merit B^2Q of the perspective haloscopes, based on the cylindrical geometry shown in [11,17] and coated with these materials, are computed and compared.

2. Physical Background

In this section, the characteristics of the high-frequency surface resistance R_s of superconductors in the mixed state are introduced. First, the electrodynamics of vortex motion are presented, and then their effects on R_s are analysed in terms of the field and the frequency dependences.

2.1. High-Frequency Vortex Motion

In the microwave frequency range, fluxons are set in oscillation around their equilibrium positions by the impinging electromagnetic (e.m.) wave. With low excitations and high frequencies (i.e., >8 GHz), as it is of interest in this case, the amplitude displacement of the vortices from their equilibrium positions is generally smaller than the intervortex spacing. Thus, in this regime, fluxons can be assumed to be non-interacting with each other, and a single-vortex motion approach can be followed to obtain the physical model [18–22].

The force (per unit length) balance equation for a single fluxon is written as:

$$\boldsymbol{J} \times (\hat{n}\Phi_0) + \boldsymbol{F}_{therm} = \eta \boldsymbol{v} + k_p \boldsymbol{u} \,, \tag{2}$$

where $\boldsymbol{J}$ is the microwave-induced current density. Its interaction with the fluxons oriented along the $\hat{n}$ direction of the magnetic field $\boldsymbol{B}$ gives rise to the driving Lorentz force that sets the fluxons in motion. $\boldsymbol{F}_{therm}$ is a stochastic force on fluxons given by thermal agitation, $\boldsymbol{v}$ is the fluxon velocity vector, $\boldsymbol{u}$ is the displacement vector of the fluxon by its pinning centre, η is the viscous drag coefficient, and k_p is the elastic recall constant representing the pinning of the fluxon on its equilibrium position.

At the temperatures of interest for the haloscopes, thermal creep effects can be neglected. Thus, by solving Equation (2), with respect to $\boldsymbol{v}$ and setting $\boldsymbol{F}_{therm} \to 0$, one obtains the vortex motion resistivity [19,21,22]:

$$\tilde{\rho}_v = \alpha \rho_{ff} \frac{1}{1 - \mathrm{i}\nu_p/\nu} \,, \tag{3}$$

where $\rho_{ff} = \Phi_0 B/\eta$ represents the resistivity of completely free vortices, known as flux-flow resistivity, and $\alpha(\phi) = \sin^2(\phi)$ [23,24] is an a-dimensional correction coefficient taking into account the mutual orientation ϕ of the field and currents ($\phi = 0$ when $\boldsymbol{J} \parallel \hat{n}$). Hence, $\tilde{\rho}_v$ is a complex quantity characterised by the characteristic frequency $2\pi\nu_p = k_p/\eta$, which separates an elastic low-frequency vortex motion regime from a highly dissipative motion regime at higher frequencies. For $\nu \gg \nu_p$, $\tilde{\rho}_v \to \rho_{ff}$. The latter can be a rather large quantity at high fields, being a fraction $\rho_{ff} \sim \rho_n B/B_{c2}$ of the normal state resistivity ρ_n, with B_{c2} being the upper critical field of the material [25,26].

In anisotropic materials (e.g., YBCO and FeSeTe) the vortex motion parameters exhibit an angular dependence given by the different properties of the material along the crystallographic directions. In case of uniaxial anisotropy, resulting from the layered structure of some superconductors, an anisotropic effective electron mass can be measured. This brings us to the definition of the anisotropy coefficient $m_c = \gamma^2 m_{ab}$, where m_c and m_{ab} are the effective masses along the c-axis (the crystallographic axis of anisotropy) and the ab-planes (a and b are the crystallographic axes normal to the c-axis), respectively, and γ is the intrinsic material anisotropy coefficient. The anisotropy on the vortex motion parameters, for high-κ SC in the London limit [25], is then derived following the Blatter–Geshkenbein–Larkin (BGL) scaling theory [27], which states that for a field- and angle- dependent observable $\mathcal{Q}(H,\theta)$, its H and θ (θ is the angle between $\boldsymbol{H}$ and the c-axis) dependences can be combined in an effective field $H\epsilon(\theta)$:

$$\mathcal{Q}(H,\theta) = s_{\mathcal{Q}}(\theta)\mathcal{Q}(H\epsilon(\theta)) \,, \tag{4a}$$

$$\epsilon(\theta) = (\gamma^{-2}\sin^2\theta + \cos^2\theta)^{1/2} \,, \tag{4b}$$

where $s_{\mathcal{Q}}(\theta)$ is an a priori known factor which depends on the particular $\mathcal{Q}(H,\theta)$: $s_\eta(\theta) = \epsilon(\theta)^{-1}$ and $s_{k_p}(\theta) = \epsilon(\theta)^{-1}$ [24,28,29]. However, it should be noted that the scaling of k_p with the BGL theory can be successfully performed only when isotropic pinning centres are present, as discussed and experimentally shown in [28]. For this reason, only samples without the addition of directional pinning centres are analysed in this paper.

Finally, when $\boldsymbol{B} \parallel \boldsymbol{J}$, i.e., $\phi = 0$, $\alpha = 0$, since the driving force acting on the fluxon $\boldsymbol{J} \times (\hat{n}\Phi_0) = 0$. However, since fluxons are magnetic structures, inside the superconductor,

the direction of the magnetic flux density field $\boldsymbol{B}$ can differ from the direction of the outer static field $\boldsymbol{H}$; hence, $\boldsymbol{B} \neq \mu_0 \boldsymbol{H}$. Indeed, also with nominally $\boldsymbol{H} \parallel \boldsymbol{J}$, it was experimentally observed that $\tilde{\rho}_v \neq 0$ [17]. This can be explained considering that the finite line tension $\varepsilon_\ell = \Phi_0^2/(4\pi\mu_0\lambda^2)$ of the fluxon lines, with λ being the London penetration depth, allows them to locally deviate from the $\boldsymbol{H}$ orientation by an angle ϕ_{loc}, so that this finite angle between $\boldsymbol{J}$ and the flux lines yields $\alpha \neq 0$. Indeed, vortex lines deform under the effects of the attractive action of pinning centres, of thermal fluctuations, and of the Lorentz force exerted by the applied currents. The latter is well-known for producing helicoidal current vortices, with the corresponding instabilities in DC regimes, and more generally, in flux-cutting phenomena [30]. In the present situation, we are considering vanishingly small, high-frequency currents whose contribution to vortex deformation and tilting, with respect to their nominal orientations, can be neglected. On the other hand, the effect of pinning centres (here considered to be point-like) and thermal fluctuations can be evaluated in a simplified way within the collective pinning theory [31]. Thanks to their finite elasticity, vortices accommodate the underlying pinning landscape to minimise the total elastic and pinning energy. In so doing, they displace by an amplitude given by the interaction length with pins ($\sim \xi$) over the so-called collective pinning length L_c. The latter identifies the length of the vortex segment, which is independently pinned with respect to the other portions of the vortex. In a simple picture, this accommodation produces a tilting angle $\phi_{loc,el} \simeq \arctan(\xi/L_c)$ between the flux line and the nominal $\boldsymbol{H}$ field orientation. The length L_c is connected to the vortex collective pinning energy $U_c \simeq \varepsilon_\ell \xi^2/L_c$. Moreover, the average amplitude of the thermal fluctuations u_{th} can be estimated by equating the thermal energy per unit length $k_B T/L_c$ to the elastic energy per unit length $(1/2)\varepsilon_\ell u_{th}^2$, due to these deformations. Thus, the tilting angle due to the thermal fluctuations is $\phi_{loc,th} \simeq \arctan(u_{th}/L_c)$. Since the two mechanisms are independent, a combined tilting angle can be computed as $\phi_{loc} \simeq \arctan(\sqrt{u_{th}^2 + \xi^2}/L_c)$. The procedure used to estimate ϕ_{loc} from the measured parameters will be detailed in Section 3.2.

This evaluation will prove useful in the following.

2.2. Surface Impedance in the Mixed State

The macroscopic material property that describes the electrodynamic response of (super)conductors is the surface impedance Z_s [32]:

$$Z_s \coloneqq E_\parallel / H_\parallel = R_s + \mathrm{i} X_s \,, \tag{5}$$

where $E_\parallel$ and $H_\parallel$ are the electric and magnetic field components parallel to the surface of the material, respectively, and $R_s \coloneqq \mathrm{Re}\, Z_s$ and $X_s \coloneqq \mathrm{Im}\, Z_s$.

In the local limit for bulk good conductors, i.e., when the thickness d of the material is much larger than the screening characteristic lengths $d \gg \min(\delta, \lambda)$, with δ being the skin penetration depth and λ being the London penetration depth, from classical electromagnetism, it can be shown that [32]:

$$Z_s = \sqrt{\mathrm{i}\omega\mu_0\tilde{\rho}} \,, \tag{6}$$

where $\omega = 2\pi\nu$ is the angular frequency of the impinging e.m. field, μ_0 is the vacuum magnetic permeability, and $\tilde{\rho}$ is the resistivity of the material, which, in the case of superconductors, is a complex quantity. The resistivity $\tilde{\rho}$ describes all the resistive and reactive phenomena in the material. Thus, for superconductors in the mixed state, the contribution of both superconducting and normal charge carriers, as well as vortex motion, must be taken into account in $\tilde{\rho}$. The interplay between the various contributions to $\tilde{\rho}$, for small displacements $\boldsymbol{u}$ of the fluxons, yields an overall resistivity which can be written as [18]:

$$\tilde{\rho} = \frac{\tilde{\rho}_v + \mathrm{i}/\sigma_2}{1 + \mathrm{i}\sigma_1/\sigma_2} \,, \tag{7}$$

where $\sigma_{2f} := \sigma_1 - i\sigma_2$ is the so-called two-fluid conductivity of superconductors [25]. This conductivity can be described as the parallel between the real conductivity of the quasi-particles σ_1 and the inductive behaviour of the superfluid $\sigma_2 \approx 1/(\omega\mu_0\lambda^2)$. Taking into account the low operative temperatures of haloscopes, since $\sigma_1 \propto x_n$ with $x_n \approx (T/T_c)^\beta$ (with $\beta = 4$ and $\beta = 2$ for low-T_c and high-T_c SC, respectively), $\sigma_1/\sigma_2 \ll 1$. Hence, Equation (7) can be approximated to $\tilde{\rho} \approx \tilde{\rho}_v + i/\sigma_2$, which yields:

$$Z_s \approx \sqrt{\omega\mu_0\left(-\frac{1}{\sigma_2} + i\tilde{\rho}_v\right)}\,. \tag{8}$$

Equation (8) will be used in the following to evaluate and compare the materials' surface resistance R_s, starting from the measurements of the vortex motion parameters, ρ_{ff} and ν_p, which define $\tilde{\rho}_v$ in Equation (3), and λ.

3. Experimental Section

In this section, the surface resistance of NbTi, Nb_3Sn, YBCO, and FeSeTe is evaluated, starting from the measurements of the vortex motion parameters. Then, the perspective performances of haloscopes coated with these materials are analysed.

To this purpose, we first show the structure of a typical haloscope, taking as a reference the haloscope presented in [11], in order to highlight the dependence of Q on the R_s of the coating layer. Then, the properties of the superconductors needed for the evaluation of R_s are collected from existing works. Finally, using the computed R_s, the sensitivity of haloscopes is evaluated to assess which of the SCs under scrutiny would give the best performances.

3.1. Haloscope Design

In this work, the superconductive haloscope presented in [11] within the QUAX experiment is used as a reference. The cavity has a cylindrical shape ($\varnothing = 26.1$ mm) with conical bases, and it is designed to operate with the applied magnetic field oriented along the main axis of the cavity. In order to facilitate the penetration of the magnetic field, the conical caps are made of copper, while the cylindrical SC body is divided in two halves by a thin copper (30 µm) layer, to break the superconducting screening currents. The transverse magnetic TM_{010} mode, which is usually employed for Primakoff axion detection in conjunction with a static magnetic field orientation parallel to the cavity axis, induces longitudinal currents on the lateral walls (thus, $\boldsymbol{H} \parallel \boldsymbol{J}$). The haloscope considered here resonates at $\nu_0 \sim 9.08$ GHz at 4 K [11]. The subscript indices of 'TM_{010}' indicate the number of the peaks of the radio frequency H-field met along the three directions of a cylindrical coordinate system: the first index '0' indicates that the H-field is constant along the azimuth direction, the second index '1' indicates that the H-field exhibits a peak along the radial direction, and the last index '0' that the H-field is constant along the axial direction (a sketch of the radio frequency fields and currents is reported in Figure 1).

Due to the different materials used for the inner coating of the cavity elements, the overall quality factor is given by:

$$\frac{1}{Q} = \frac{R_{s,cyl}}{G_{cyl}} + \frac{R_{s,cones}}{G_{cones}}\,, \tag{9}$$

where, for this cavity, $G_{cyl} \simeq 482\ \Omega$ and $G_{cones} \simeq 6270\ \Omega$ are the geometrical factors of the cylindrical body and conical caps, respectively, and $R_{s,cyl}$ and $R_{s,cones}$ are their surface resistances. At 9.08 GHz and 4 K, in the anomalous skin depth regime [33], the surface resistance of copper is $R_{s,Cu} \simeq 4.9\ m\Omega$. Thus, a cavity with this geometry, entirely made of copper, would have $Q_{min} \simeq 9.1 \times 10^4$ at 9 GHz. This is the lower limit given by copper that we expect to be outperformed by the use of superconductive coatings, whereas, in the ideal case for which $R_{s,cyl}/G_{cyl}$ can be neglected, the upper limit $Q_{max} \simeq 1.3 \times 10^6$ could be reached with this geometry. Thus, the highest performance increase in the B^2Q figure of merit reachable with this haloscope geometry is $Q_{max}/Q_{min} = G_{cones}/G_{cyl} + 1 \approx 14$.

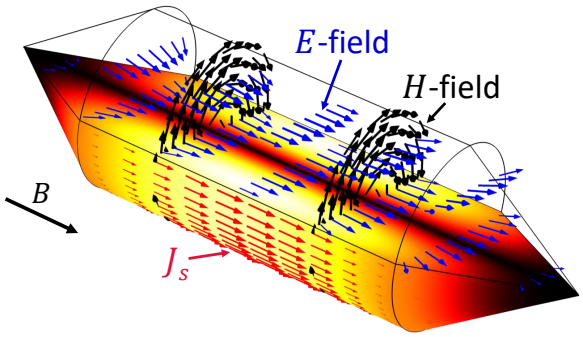

Figure 1. Electromagnetic simulation of the haloscope excited with the TM_{010} mode. The distributions of the radio frequency electric *E*-field (in blue), the magnetic *H*-field (in black), and the surface current density J_s (in red) are shown. The direction of the externally applied static *B* field is shown to be parallel to the longitudinal axis of the cavity.

3.2. Materials under Investigation

The perspective application of four different superconductive materials to the realisation of haloscopes is investigated here.

In Table 1, the list of the samples, whose vortex motion parameters were measured in high magnetic fields, their main characteristics, and references where further information can be found, are reported.

Table 1. List of the samples under investigation.

Material	**NbTi**	**Nb_3Sn**	**$YBa_2Cu_3O_{7-\delta}$**	**$FeSe_{0.5}Te_{0.5}$**
Thickness (nm)	$(3.5 \pm 0.5) \times 10^3$	bulk	80 ± 5	240 ± 15
Growing tech.	RF sputtering	HIP (1)	CSD (2)	PLD (3)
Substrate	Cu	–	$LaAlO_3$	CaF_2
T_c (K)	8.0 ± 0.2	18.0 ± 0.2	89.9 ± 0.5	18.0 ± 0.2
Ref.	[11]	[16,34]	[35]	[36]

(1) High Isostatic Pressure; (2) Chemical Solution Deposition; (3) Pulsed Laser Deposition.

The microwave vortex motion properties of NbTi were characterised through the study of the performance of the NbTi-coated haloscope analysed in [11]. The Nb_3Sn, YBCO, and FeSeTe samples were studied through the measurement technique based on the use of the dielectric loaded resonator described and optimised in [37–40]. In particular, the analysis of the vortex motion parameters in Nb_3Sn was reported in [16,41]. The microwave surface impedance analysis, limited to $B \leq 1.2$ T, of FeSeTe was detailed in [29,42,43], while both the FeSeTe and YBCO data in high magnetic fields were specifically measured for this work.

For the comparison, we chose to work in the same operative condition of the cavity analysed in [11]: $T = 4$ K, $\mu_0 H = 5$ T parallel to the SC surface, and with the selected resonant mode inducing microwave currents $\boldsymbol{J} \parallel \boldsymbol{H}$. Actually, the latter samples (Nb_3Sn, YBCO, and FeSeTe) were characterised with a different configuration of currents and field orientations ($\boldsymbol{J} \perp \boldsymbol{H}$ with $\boldsymbol{H} \parallel c$-axis for anisotropic SC), with respect to the haloscope considered here. Hence, the vortex motion resistivity $\tilde{\rho}$ must be properly evaluated in the configuration of interest. First, the α coefficient must be evaluated; see Equation (3). This is accomplished through the first-order model proposed in Section 2. The collective pinning length $L_c = \sqrt{2\varepsilon_\ell / k_p}$ is evaluated from the experimentally measured k_p by equating the pinning energy U_c / L_c to the pinning energy (both per unit length) expressed in terms of k_p, $k_p \xi^2 / 2$. The data used to estimate L_c and ε_ℓ, i.e., λ and k_p, are reported in Table 2.

Second, for both YBCO and FeSeTe, the intrinsic material anisotropy must be taken into account (see Equation (4)), taking γ from [28,42] for YBCO and FeSeTe, respectively.

The anisotropy enters also the evaluation of the α coefficient, which, in the geometry here considered, enhances tilting due to thermal fluctuations and reduces the one due to the elastic accommodation to pins. It is worth noting here that FeSeTe is a multiband superconductor. Indeed, it exhibits intricate anisotropy properties which are actually different among the various superconducting quantities λ, ξ, B_{c1}, and B_{c2} [44]. Moreover, ρ_{ff} shows an unusual field dependence [29,42,43,45]. Hence, a direct experimental study of FeSeTe in the same configuration involved in the considered haloscope design would be particularly recommended.

In addition, for the sake of simplicity, we neglect the increased pinning when $\boldsymbol{H} \parallel ab$ planes (the so-called 'intrinsic pinning'), which is connected to the layered structure of materials such as YBCO. Moreover, it must be noted that, in engineered materials, the effects of the intrinsic pinning are essentially hidden by those of the artificial pinning centres [28].

Finally, the T and H range of interest must be considered. Since measurements at $T = 4$ K and $\mu_0 H = 5$ T are available only for Nb_3Sn, for YBCO and FeSeTe, the low-temperature data must be extrapolated from currently existing measurements. However, the temperature dependences of both η and k_p derive from those of λ and of the coherence length ξ [46]: hence, at low temperatures, these parameters saturate similarly to λ and ξ [25]. Thus, negligible uncertainties associated with the model choice are introduced in the mentioned extrapolation [46].

The pinning frequency is computed from k_p and η as $2\pi\nu_p = k_p/\eta$. In Figure 2a the pinning constant $k_p(t)$, with $t = T/T_c$, measured at 5 T on YBCO and FeSeTe is shown. The measurements are obtained in zero field cooling (ZFC) conditions by sweeping the magnetic field at fixed temperature values. The values at 4 K are extrapolated from these measurements through the empirical models shown in [46] and reported in the caption of Figure 2. The field dependence of k_p is shown in Figure 2b. Here, the Nb_3Sn measurement, performed at 4 K (thus for it no extrapolation is needed), is also reported. From the behavior of $k_p(H)$ on the different materials, different pinning regimes can be recognised. In YBCO, k_p is field-independent at 10 K and up to 10 T, indicating a pinning regime where fluxons are strongly pinned, independently one from another. On the contrary, FeSeTe and Nb_3Sn display a $k_p \propto H^{-0.5}$ dependence, typical of the collective pinning regime (bundles of fluxons pinned on multiple pinning centres). These field dependences will be considered in the final performance analysis presented.

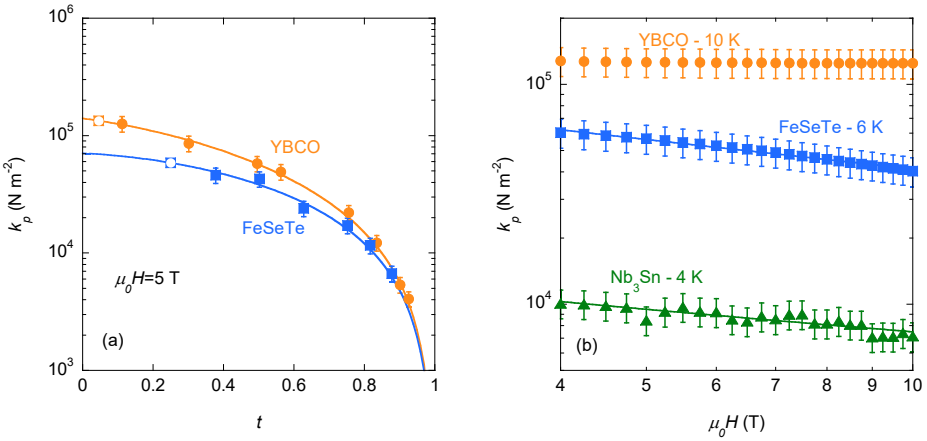

Figure 2. (**a**) Pinning constant k_p, measured on YBCO (orange circles) and FeSeTe (blue squares) in zero field cooling conditions (ZFC) at 5 T as a function of the reduced temperature $t = T/T_c$. The fit of the data is performed with the model developed in [46]: $k_p(t) = k_p(0)(1-t)^{4/3}(1+t)^2 e^{(-T/T_0)}$. The best fit parameters are: $k_p(0) = 1.40 \times 10^5$ N m^{-2} and $T_0 = 56$ K for YBCO, $k_p(0) = 7.07 \times 10^4$ N m^{-2} and $T_0 = T_c$ for FeSeTe. The empty square symbols represent the points extrapolated from the fit at 4 K (which will be used in the next elaborations). (**b**) Field dependence of k_p in Nb_3Sn (green triangle), YBCO, and FeSeTe samples measured at the lower temperatures. $k_p(H)$ in Nb_3Sn and FeSeTe is shown to be $\propto H^{-0.5}$.

For what concerns $\eta = \Phi_0 B/\rho_{ff}$, in Figure 3, measurements at 5 T on YBCO and FeSeTe are reported. Additionally, in this case, from the model shown in [46], the value at 4 K is extrapolated. Resorting to the conventional Bardeen–Stephen behaviour [26] exhibited by Nb_3Sn [16] and NbTi, the flux-flow resistivity is simply obtained from the normal state resistivity ρ_n as $\rho_{ff} = \rho_n B/B_{c2}$ with $B_{c2} \approx B_{c2}(0)(1-t^2)$. We take $\rho_n = 14.8$ μΩ cm and $B_{c2} = 27$ T for Nb_3Sn [16], and $\rho_n = 70$ μΩ cm, $B_{c2} = 13$ T for NbTi [11].

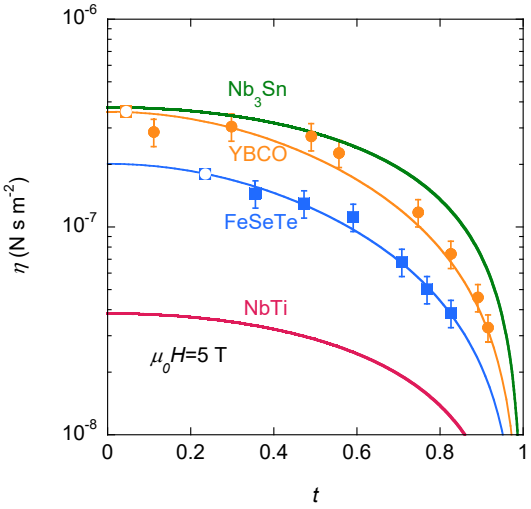

Figure 3. Viscous drag coefficient η measured on YBCO (orange circles) and FeSeTe (blue squares) at 5 T in ZFC as a function of the reduced temperature t. The measured data are approximated with $\eta(t) = \eta(0)(1-t^2)/(1+t^2)$ [46], with $\eta(0) = 3.59 \times 10^{-7}$ N s m^{-2} for YBCO and $\eta(0) = 2.02 \times 10^{-7}$ N s m^{-2} for the FeSeTe sample. The empty square symbols represent the points extrapolated from the fit at 4 K (which will be used in the next elaborations). The green and red curves represent $\eta(t)$ obtained by considering $\eta(t) = \Phi_0 B_{c2}(t)/\rho_n$ (from $\rho_{ff} = \rho_n B/B_{c2}$ and $\eta = \Phi_0 B/\rho_{ff}$) for Nb_3Sn and NbTi, respectively.

All the parameters of interest for the different materials are reported in Table 2.

Table 2. Measured parameters of the SCs of interest used for the evaluation of R_s.

	NbTi	**Nb_3Sn**	**YBCO**	**FeSeTe**
k_p (N m^{-2}) at 4 K, 5 T	–	$(9.9 \pm 1.5) \times 10^3$	$(1.3 \pm 0.2) \times 10^5$	$(5.9 \pm 0.9) \times 10^4$
pinning regime	single	collective	single	collective
η (N s m^{-2}) at 4 K, 5 T	–	–	$(3.6 \pm 0.5) \times 10^{-7}$	$(1.8 \pm 0.3) \times 10^{-7}$
ρ_n (μΩ cm)	70 ± 2	14.8 ± 0.2	–	–
$B_{c2}(0)$ (T)	13.0 ± 0.5	27.0 ± 0.5	–	–
ν_p (GHz) at 4 K, 5 T	44 ± 7	4.2 ± 0.6	59 ± 9	52 ± 8
meas. geometry	$\boldsymbol{H} \parallel \boldsymbol{J}$	$\boldsymbol{H} \perp \boldsymbol{J}$	$\boldsymbol{H} \parallel c$ axis, $\boldsymbol{H} \perp \boldsymbol{J}$	
γ	1	1	5.3 ± 0.7	1.8 ± 0.2
$\lambda(0)$ (nm)	270 ± 20 [17,47]	160 ± 20 [48]	150 ± 10 [49,50]	520 ± 50 [45]

4. Results and Discussion

From the data collected in Table 2, the surface resistance R_s of the selected SCs is evaluated to compare the figure of merit B^2Q of haloscopes (with the geometry shown in [11]) and coated with different materials. In particular, Equation (3) is computed with the data in Table 2, taking into account the α coefficient, the anisotropy γ for YBCO and FeSeTe, the collective pinning dependences in Nb_3Sn and FeSeTe, and the pair-breaking effects on the superfluid σ_2 and, for NbTi, also on σ_1. From this, the complex resistivity $\tilde{\rho}$

from Equation (7) and R_s from Equation (6) are obtained. Finally, the Q of the haloscope is computed using Equation (9).

The performances comparison is based on the figure of merit B^2Q. In Figure 4, the field dependences of B^2Q of the different haloscopes are shown at 4 K and 9.08 GHz. Both a lower worst-case limit, obtained considering fluxons aligned in the *ab* planes (for the anisotropic SC) and $\boldsymbol{B} \perp \boldsymbol{J}$, and an upper limit, obtained with the α coefficients evaluated as shown in Section 2, are given. It can be seen that, in the worst case, both Nb_3Sn and NbTi exhibit a lower B^2Q than that given by a Cu cavity, while both YBCO and FeSeTe have, even in this case, a B^2Q higher than that of Cu. In the more realistic scenario given by the upper limits shown in Figure 4, all the SC studied here are better than Cu. Table 3 reports the numerical evaluation of the performances at 5 T, where it can be seen that $(B^2Q)_{\mathrm{YBCO}}/(B^2Q)_{\mathrm{Cu}}$ is close to the upper limit of 14, which is reachable with the analysed geometry. At the highest B, the NbTi performance starts dropping due its lower B_{c2}. With respect to YBCO, FeSeTe exhibits similar performances despite its lower η and k_p, because its large λ helps to reduce R_s in the bulk limit, as can be deduced from Equation (8).

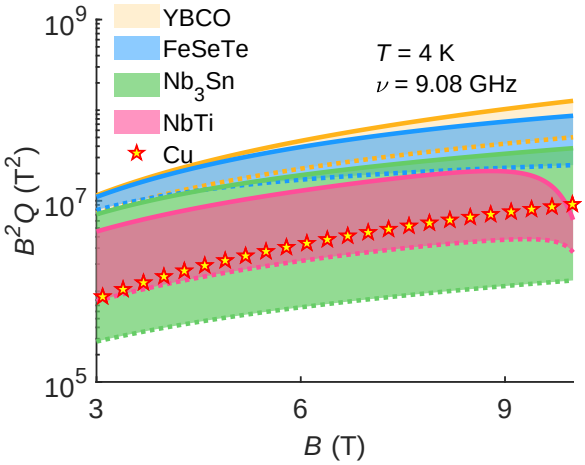

Figure 4. Comparison of the B^2Q factors evaluated at 4 K and 9.08 GHz as a function of B. The dotted lines represent the worst lower limit obtained in the $\boldsymbol{B} \perp \boldsymbol{J}$ configuration. The continuous lines represent a more realistic situation, for which the α angular coefficient is taken into account, as is explained in the text. The 'star' symbols represent the B^2Q values obtained with a Cu cavity, the yellow area represents the values obtainable with YBCO, the light blue area represents those with FeSeTe, the green area represents those with Nb_3Sn, and the red area represents those with NbTi.

Since, at a fixed signal to noise ratio (SNR), bandwidth detection, and system temperature, the integration time is $t_i \propto P_{a\to\gamma_{ph}}^{-2}$, the increase of (B^2Q) shown in Table 3 can be directly read as an equivalent reduction in t_i [10].

The frequency dependence $B^2Q(\nu)$, reported in Figure 5 for $10^9 < \nu/(\mathrm{Hz}) < 10^{11}$ at 5 T and 4 K, shows interesting features that can be used to assess the best material in the different bands. It can be seen that, given the low ν_p of Nb_3Sn, the Q of the associated haloscope is expected to decrease at frequencies lower than in the other materials. However, thanks to the low ρ_n and high B_{c2} of Nb_3Sn, with respect to NbTi, the figure of merit of the Nb_3Sn haloscope tends to settle on higher values at high frequencies, where $\tilde{\rho}_v$ saturates at ρ_{ff}. Thus, Nb_3Sn is more convenient than NbTi for $\nu > 10$ GHz and, at even higher frequencies, its performances could be comparable with those of YBCO and FeSeTe. This result highlights clearly that for high-frequency applications of SC in the mixed state, not only a high ν_p is desirable, but also a low ρ_{ff} is important.

Table 3. Comparison of the (B^2Q) figure of merit of the different materials, with respect to that of Cu at 5 T, 4 K, 9.08 GHz.

Material	$(B^2Q)/(B^2Q)_{Cu}$	$t_i/t_{i,Cu}$
NbTi	4.3	0.05
Nb_3Sn	6.5	0.02
FeSeTe	12	0.006
YBCO	14	0.005

For what concerns the frequency dependence of $B^2Q(\nu)$ for FeSeTe and YBCO, it can be noted that the worst-case lower limits of B^2Q follow the same frequency behaviour due to their similar ν_p. The upper B^2Q limits follow a $\nu^{2/3}$ dependence (typical of the anomalous skin depth regime exhibited by Cu) for $\nu < 10$ GHz for both YBCO and FeSeTe. In fact, with these materials, at the lower frequencies, the cavity losses are dominated by the copper bases. At higher frequencies, the losses in YBCO still do not contribute substantially to the overall Q, while with FeSeTe, the Q starts decreasing more rapidly than in the Cu cavity.

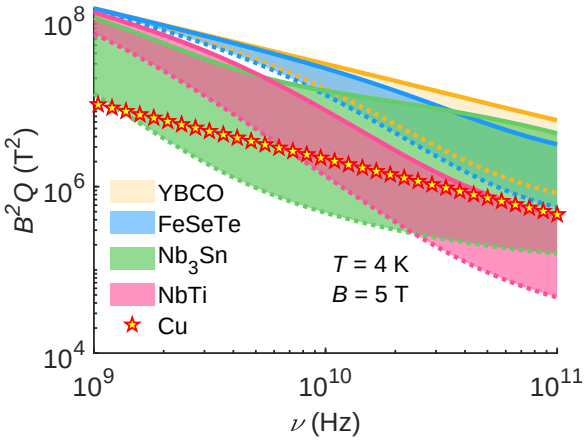

Figure 5. Comparison of the B^2Q factors evaluated at 4 K and 5 T as a function of ν and keeping the same geometrical factors as in Section 3.1. The dotted lines represent the worst lower limit obtained in the $\boldsymbol{B} \perp \boldsymbol{J}$ configuration. The continuous lines represent a more realistic situation, for which the α angular coefficient is taken into account, as is explained in the text. The 'star' symbols represent the B^2Q values obtained with a Cu cavity, the yellow area represents the values obtainable with YBCO, the light blue area represents those with FeSeTe, the green area represents those with Nb_3Sn, and the red area represents those with NbTi.

5. Conclusions

In this paper, the impact of the vortex motion and screening properties of different superconducting materials (i.e., NbTi, Nb_3Sn, YBCO, and FeSeTe) on the performances of haloscopes, in terms of the power of the detected signal, was evaluated.

In particular, the comparison of the B^2Q figure of merit of haloscopes in the hybrid geometry proposed in [11] has been completed by evaluating the $Q(B, \nu)$ as determined by the surface resistance $R_s(B, \nu)$ behaviour of the aforementioned SC.

In turn, the R_s of these SC was computed, starting from the vortex motion parameters measured at microwave frequencies and high magnetic fields. The effect on fluxon pinning by the different orientations of the static magnetic field $\boldsymbol{B}$, with respect to the induced microwave currents imposed by the specific haloscope geometry, was taken into account.

The results show that, even at 5 T and at low frequencies $\nu < 10$ GHz, all the studied materials allow an increase of the haloscope sensitivity with respect to Cu, while, at higher frequencies, NbTi becomes unsuitable, and Nb_3Sn can still be a useful solution, despite

its lower ν_p. Interestingly, FeSeTe, which here is, for the first time, considered for this application, can be a promising material for the inner coating of haloscopes, despite its high vortex motion dissipation. Indeed, its large λ contributes to lowering the bulk R_s, allowing it to reach performances obtained with YBCO. Moreover, one has to consider that Iron-based SCs are still far from the optimisation and maturity levels reached with YBCO, thus allowing further room for improvements.

Finally, YBCO is shown to be the best choice, leading to an increase of the measurement sensitivity by a factor of ∼14, with respect to the Cu cavity in the whole analysed frequency range (i.e., $10^9 < \nu/(\mathrm{Hz}) < 10^{11}$). This result is close to the maximum theoretical increase in the sensitivity reachable with the haloscope geometry studied.

To conclude, despite the expected high performances of YBCO in the operative conditions of haloscopes, this study shows the possibility to also employ other SCs, in selected frequency bands, to increase the sensitivity of these axion detectors.

Author Contributions: Conceptualisation, A.A., N.P., E.S. and K.T.; methodology, A.A. and N.P.; validation, A.A., N.P. and K.T.; formal analysis, A.A. and N.P.; investigation, A.A., D.D.G., N.P. and K.T.; data curation, A.A., D.D.G., N.P. and K.T.; writing—original draft preparation, A.A. and N.P.; writing—review and editing, D.D.G., C.G., E.S. and K.T.; visualisation, A.A.; supervision, C.G., N.P. and E.S; project administration, C.G. and E.S.; funding acquisition, E.S. All authors have read and agreed to the published version of the manuscript.

Funding: This work was partially supported by the MIUR-PRIN project 'HIBiSCUS'—grant No. 201785KWLE, and by the INFN—Commissione Scientifica Nazionale 5 project 'SAMARA'.

Institutional Review Board Statement: Not applicable.

Informed Consent Statement: Not applicable.

Data Availability Statement: Data are provided in the figures and tables of the article. Data files are available upon request to the corresponding author.

Acknowledgments: The authors acknowledge C. Pira for the NbTi coating of the copper cavities, T. Spina and R. Flükiger for the Nb_3Sn sample, V. Pinto and G. Celentano for the YBCO sample, and G. Sylva and V. Braccini for the FeSeTe sample.

Conflicts of Interest: The authors declare no conflict of interest.

References

1. Peccei, R.D.; Quinn, H.R. CP conservation in the presence of pseudoparticles. *Phys. Rev. Lett.* **1977**, *38*, 1440. [CrossRef]
2. Wilczek, F. Problem of Strong P and T Invariance in the Presence of Instantons. *Phys. Rev. Lett.* **1978**, *40*, 279. [CrossRef]
3. Weinberg, S. A new light boson? *Phys. Rev. Lett.* **1978**, *40*, 223. [CrossRef]
4. Primakoff, H. Photo-production of neutral mesons in nuclear electric fields and the mean life of the neutral meson. *Phys. Rev.* **1951**, *81*, 899. [CrossRef]
5. Tanabashi, M.; Hagiwara, K.; Hikasa, K.; Nakamura, K.; Sumino, Y.; Takahashi, F.; Tanaka, J.; Agashe, K.; Aielli, G.; Amsler, C.; et al. Review of particle physics. *Phys. Rev. D* **2018**, *98*, 030001. [CrossRef]
6. Preskill, J.; Wise, M.B.; Wilczek, F. Cosmology of the invisible axion. *Phys. Lett. B* **1983**, *120*, 127. [CrossRef]
7. Abbott, L.F.; Sikivie, P. A cosmological bound on the invisible axion. *Phys. Lett. B* **1983**, *120*, 133. [CrossRef]
8. Dine, M.; Fischler, W. The not so harmless axion. *Phys. Lett. B* **1983**, *120*, 137. [CrossRef]
9. Sikivie, P. Experimental tests of the "invisible" axion. *Phys. Rev. Lett.* **1983**, *51*, 1415. [CrossRef]
10. Braine, T.; Cervantes, R.; Crisosto, N.; Du, N.; Kimes, S.; Rosenberg, L.; Rybka, G.; Yang, J.; Bowring, D.; Chou, A.; et al. Extended search for the invisible axion with the axion dark matter experiment. *Phys. Rev. Lett.* **2020**, *124*, 101303. [CrossRef] [PubMed]
11. Alesini, D.; Braggio, C.; Carugno, G.; Crescini, N.; D'Agostino, D.; Di Gioacchino, D.; Di Vora, R.; Falferi, P.; Gallo, S.; Gambardella, U.; et al. Galactic axions search with a superconducting resonant cavity. *Phys. Rev. D* **2019**, *99*, 101101. [CrossRef]
12. Ahn, D.; Kwon, O.; Chung, W.; Jang, W.; Lee, D.; Lee, J.; Youn, S.W.; Youm, D.; Semertzidis, Y.K. Superconducting cavity in a high magnetic field. *arXiv* **2020**, arXiv:2002.08769.
13. Golm, J.; Cuendis, S.A.; Calatroni, S.; Cogollos, C.; Döbrich, B.; Gallego, J.; Barceló, J.; Granados, X.; Gutierrez, J.; Irastorza, I.; et al. Thin Film (High Temperature) Superconducting Radiofrequency Cavities for the Search of Axion Dark Matter. *arXiv* **2021**, arXiv:2110.01296.

14. Alesini, D.; Braggio, C.; Carugno, G.; Crescini, N.; D'Agostino, D.; Di Gioacchino, D.; Di Vora, R.; Falferi, P.; Gambardella, U.; Gatti, C.; et al. Realization of a high quality factor resonator with hollow dielectric cylinders for axion searches. *Nucl. Instrum. Methods Phys. Res. A* **2021**, *985*, 164641. [CrossRef]
15. Alesini, D.; Braggio, C.; Carugno, G.; Crescini, N.; D'Agostino, D.; Di Gioacchino, D.; Di Vora, R.; Falferi, P.; Gambardella, U.; Gatti, C.; et al. High quality factor photonic cavity for dark matter axion searches. *Rev. Sci. Instrum.* **2020**, *91*, 094701. [CrossRef]
16. Alimenti, A.; Pompeo, N.; Torokhtii, K.; Spina, T.; Flükiger, R.; Muzzi, L.; Silva, E. Microwave measurements of the high magnetic field vortex motion pinning parameters in Nb_3Sn. *Supercond. Sci. Technol.* **2020**, *34*, 014003. [CrossRef]
17. Di Gioacchino, D.; Gatti, C.; Alesini, D.; Ligi, C.; Tocci, S.; Rettaroli, A.; Carugno, G.; Crescini, N.; Ruoso, G.; Braggio, C.; et al. Microwave losses in a dc magnetic field in superconducting cavities for axion studies. *IEEE Trans. Appl. Supercond.* **2019**, *29*, 1–5. [CrossRef]
18. Coffey, M.W.; Clem, J.R. Unified theory of effects of vortex pinning and flux creep upon the rf surface impedance of type-II superconductors. *Phys. Rev. Lett.* **1991**, *67*, 386. [CrossRef] [PubMed]
19. Gittleman, J.I.; Rosenblum, B. Radio-frequency resistance in the mixed state for subcritical currents. *Phys. Rev. Lett.* **1966**, *16*, 734. [CrossRef]
20. Wu, D.H.; Booth, J.; Anlage, S.M. Frequency and field variation of vortex dynamics in $YBa_2Cu_3O_{7-\delta}$. *Phys. Rev. Lett.* **1995**, *75*, 525. [CrossRef] [PubMed]
21. Pompeo, N.; Silva, E. Reliable determination of vortex parameters from measurements of the microwave complex resistivity. *Phys. Rev. B* **2008**, *78*, 094503. [CrossRef]
22. Pompeo, N.; Alimenti, A.; Torokhtii, K.; Silva, E. Physics of vortex motion by means of microwave surface impedance measurements. *Low Temp. Phys.* **2020**, *46*, 343. [CrossRef]
23. Pompeo, N. Analysis of Pinning in the Linear AC Response of Anisotropic Superconductors in Oblique Magnetic Fields. *J. Appl. Phys.* **2015**, *117*, 103904. [CrossRef]
24. Pompeo, N.; Silva, E. Analysis of the Measurements of Anisotropic AC Vortex Resistivity in Tilted Magnetic Fields. *IEEE Trans. Appl. Supercond.* **2018**, *28*, 8201109. [CrossRef]
25. Tinkham, M. *Introduction to Superconductivity*; Dover Publications: Dover, NY, USA, 2004.
26. Bardeen, J.; Stephen, M. Theory of the motion of vortices in superconductors. *Phys. Rev.* **1965**, *140*, A1197. [CrossRef]
27. Blatter, G.; Geshkenbein, V.B.; Larkin, A. From isotropic to anisotropic superconductors: A scaling approach. *Phys. Rev. Lett.* **1992**, *68*, 875. [CrossRef]
28. Pompeo, N.; Alimenti, A.; Torokhtii, K.; Bartolomé, E.; Palau, A.; Puig, T.; Augieri, A.; Galluzzi, V.; Mancini, A.; Celentano, G.; et al. Intrinsic anisotropy and pinning anisotropy in nanostructured $YBa_2Cu_3O_{7-\delta}$ from microwave measurements. *Supercond. Sci. Technol.* **2020**, *33*, 044017. [CrossRef]
29. Pompeo, N.; Torokhtii, K.; Alimenti, A.; Sylva, G.; Braccini, V.; Silva, E. Pinning properties of FeSeTe thin film through multifrequency measurements of the surface impedance. *Supercond. Sci. Technol.* **2020**, *33*, 114006. [CrossRef]
30. Campbell, A.M. Flux Cutting in Superconductors. *Supercond. Sci. Technol.* **2011**, *24*, 091001. [CrossRef]
31. Blatter, G.; Feigel'man, M.; Geshkenbein, V.; Larkin, A.; Vinokur, V. Vortices in High-Temperature Superconductors. *Rev. Mod. Phys.* **1994**, *66*, 1125. [CrossRef]
32. Collin, R.E. *Foundations for Microwave Engineering*; John Wiley & Sons: Hoboken, NJ, USA, 2007.
33. Reuter, G.; Sondheimer, E. The theory of the anomalous skin effect in metals. *Proc. R. Soc. Lond.* **1948**, *195*, 336. [CrossRef]
34. Flükiger, R.; Spina, T.; Cerutti, F.; Ballarino, A.; Scheuerlein, C.; Bottura, L.; Zubavichus, Y.; Ryazanov, A.; Svetogovov, R.; Shavkin, S.; et al. Variation of $T_c c$, lattice parameter and atomic ordering in Nb_3Sn platelets irradiated with 12 MeV protons: Correlation with the number of induced Frenkel defects. *Supercond. Sci. Technol.* **2017**, *30*, 054003. [CrossRef]
35. Pinto, V.; Vannozzi, A.; Angrisani Armenio, A.; Rizzo, F.; Masi, A.; Santoni, A.; Meledin, A.; Ferrarese, F.M.; Orlanducci, S.; Celentano, G. Chemical Solution Deposition of YBCO Films with Gd Excess. *Coatings* **2020**, *10*, 860. [CrossRef]
36. Braccini, V.; Kawale, S.; Reich, E.; Bellingeri, E.; Pellegrino, L.; Sala, A.; Putti, M.; Higashikawa, K.; Kiss, T.; Holzapfel, B.; et al. Highly effective and isotropic pinning in epitaxial Fe(Se,Te) thin films grown on CaF_2 substrates. *Appl. Phys. Lett.* **2013**, *103*, 172601. [CrossRef]
37. Alimenti, A.; Torokhtii, K.; Silva, E.; Pompeo, N. Challenging microwave resonant measurement techniques for conducting material characterization. *Meas. Sci. Technol.* **2019**, *30*, 065601. [CrossRef]
38. Torokhtii, K.; Pompeo, N.; Silva, E.; Alimenti, A. Optimization of Q-factor and resonance frequency measurements in partially calibrated resonant systems. *Meas. Sens.* **2021**, *18*, 100314. [CrossRef]
39. Torokhtii, K.; Alimenti, A.; Pompeo, N.; Leccese, F.; Orsini, F.; Scorza, A.; Sciuto, S.; Silva, E. Q-factor of microwave resonators: Calibrated vs. uncalibrated measurements. *J. Phys. Conf. Ser.* **2018**, *1065*, 052027.
40. Alimenti, A.; Pompeo, N.; Torokhtii, K.; Silva, E. Surface Impedance Measurements in Superconductors in DC Magnetic Fields: Challenges and Relevance to Particle Physics Experiments. *IEEE Instrum. Meas. Mag.* **2021**, *24*, 12. [CrossRef]
41. Alimenti, A.; Pompeo, N.; Torokhtii, K.; Spina, T.; Flükiger, R.; Muzzi, L.; Silva, E. Surface Impedance Measurements on Nb_3Sn in High Magnetic Fields. *IEEE Trans. Appl. Supercond.* **2019**, *29*, 3500104. [CrossRef]
42. Pompeo, N.; Alimenti, A.; Torokhtii, K.; Sylva, G.; Braccini, V.; Silva, E. Pinning, Flux Flow Resistivity, and Anisotropy of Fe(Se,Te) Thin Films From Microwave Measurements Through a Bitonal Dielectric Resonator. *IEEE Trans. Appl. Supercond.* **2021**, *31*, 8000805. [CrossRef]

43. Pompeo, N.; Alimenti, A.; Torokhtii, K.; Sylva, G.; Braccini, V.; Silva, E. Microwave properties of Fe(Se,Te) thin films in a magnetic field: pinning and flux flow. *J. Phys. Conf. Ser.* **2020**, *1559*, 012055.
44. Bendele, M.; Weyeneth, S.; Puzniak, R.; Maisuradze, A.; Pomjakushina, E.; Conder, K.; Pomjakushin, V.; Luetkens, H.; Katrych, S.; Wisniewski, A.; et al. Anisotropic superconducting properties of single-crystalline $FeSe_{0.5}Te_{0.5}$. *Phys. Rev. B* **2010**, *81*, 224520. [CrossRef]
45. Okada, T.; Nabeshima, F.; Takahashi, H.; Imai, Y.; Maeda, A. Exceptional suppression of flux-flow resistivity in $FeSe_{0.4}Te_{0.6}$ by back-flow from excess Fe atoms and Se/Te substitutions. *Phys. Rev. B* **2015**, *91*, 054510. [CrossRef]
46. Golosovsky, M.; Tsindlekht, M.; Davidov, D. High-frequency vortex dynamics in. *Supercond. Sci. Technol.* **1996**, *9*, 1. [CrossRef]
47. Benvenuti, C.; Calatroni, S.; Hauer, M.; Minestrini, M.; Orlandi, G.; Weingarten, W. (NbTi)N and NbTi coatings for superconducting accelerating cavities. In Proceedings of the Fifth Workshop RF on RF Superconductivity, Hamburg, Germany, 19–24 August 1991; pp. 518–526.
48. Posen, S.; Liepe, M. Advances in development of Nb_3Sn superconducting radio-frequency cavities. *Phys. Rev. Accel. Beams* **2014**, *17*, 112001. [CrossRef]
49. Sonier, J.; Kiefl, R.; Brewer, J.; Bonn, D.; Carolan, J.; Chow, K.; Dosanjh, P.; Hardy, W.; Liang, R.; MacFarlane, W.; et al. New muon-spin-rotation measurement of the temperature dependence of the magnetic penetration depth in $YBa_2Cu_3O_{6.95}$. *Phys. Rev. Lett.* **1994**, *72*, 744. [CrossRef] [PubMed]
50. Tallon, J.; Bernhard, C.; Binninger, U.; Hofer, A.; Williams, G.; Ansaldo, E.; Budnick, J.; Niedermayer, C. In-Plane Anisotropy of the Penetration Depth Due to Superconductivity on the Cu-O Chains in $YBa_2Cu_3O_{7-\delta}$, $YBa_2Cu_3O_{15-\delta}$, and $YBa_2Cu_3O_8$. *Phys. Rev. Lett.* **1995**, *74*, 1008. [CrossRef]